Reservoir characterization using oil-production-induced microseismicity, Clinton County, Kentucky

James T. Rutledge, Nambe Geophysical, Inc., jrutledge@lanl.gov

W. Scott Phillips, Nambe Geophysical, Inc., wsp@lanl.gov

Barbra K. Schuessler, Los Alamos National Laboratory, schuess@seismo5.lanl.gov

Text and figures can be accessed at: http://www.ees4.lanl.gov/microeq

Abstract

Microseismic monitoring tests were conducted from 1993 to 1995 in the Seventy-Six oil field, Clinton County, Kentucky. Oil is produced from low-porosity, fractured carbonate rocks at <600 m depth. Downhole geophones were deployed in wells located within 120 to 250 m of new production wells. Three tests were conducted sequentially for $9^1/2$, $20^1/2$, and 30 week periods during which 110, 180 and 3237 microearthquakes were detected, respectively. Moment-derived magnitudes ranged from -2.5 to 0.9. Volumes extracted ranged from about 1300 to 1800 m^3; no injection operations were conducted. Gross changes in production rate correlate with event rate; event rate lags changes in production rate by 2 to 3 weeks. Hypocenters and first-motion data have revealed previously undetected, low-angle thrust faults above and below the currently-drained depth intervals. Production history, well logs and drill tests indicate the seismically-active faults or fractures are previously-drained intervals that have subsequently recovered to hydrostatic pressure via brine invasion. Storage capacity computed for one of these drained fractures implies total oil production represents about 20% of total pore volume. Correlation of older production intervals and well-log porosity anomalies with the seismically-active faults indicate the oil reservoir in the study area is primarily a set of compartmentalized, low-angle thrust faults. Although low-angle fracture sets have not previously been considered in the exploration and development of the area, the mapped thrust faults are consistent with other investigators' interpretations of oil associated with secondary fracture sets occurring along deeper-seated, wrench-fault structures.

Stress determined from composite focal mechanisms indicates a near-surface (<550 m) thrust regime. Maximum horizontal stress direction is N15°W ±15°, rotated approximately 90° from regional orientation. The seismic behavior is consistent with poroelastic models that predict slight increases in horizontal compressive stress above and below currently-drained volumes. Pressure re-equilibration via brine invasion replacing previously-produced oil along the seismically-active faults should also be weakly promoting the observed seismic failure. Total estimated production-induced stress change promoting slip is approximately 0.02 MPa.

Introduction

The technique of mapping conductive fractures using induced microseismicity has been successfully applied in several hydraulic fracture operations (e.g. Albright and Pearson, 1982; Batchelor et al., 1983; Fehler et al., 1986; Vinegar et al., 1991; Block et al., 1994; Keck and Withers; 1994, Warpinski et al., 1995; Cornet and Jianmin, 1995; Phillips et al., 1998). Induced seismicity and faulting has also been associated with subsurface fluid extraction (e.g. Yerkes and Castle, 1976; Eberhart-Phillips and Oppenheimer, 1984; Pennington et al., 1986; Segall, 1989; Grasso and Wittlinger, 1990; Teufel et al., 1991; Doser et al., 1991; Grasso, 1992) and more complex operations involving sequential or simultaneous extraction and pressure recovery operations (e.g. Niitsuma et al., 1987; Davis and Pennington, 1989; Teufel and Rhett, 1992; Rutledge et al., 1994a; Deflandre et al., 1995). In this paper we demonstrate an application of mapping natural, conductive reservoir fractures on an interwell scale (100's of meters) using oil-production induced microearthquakes. Three successful monitoring tests were conducted from 1993 to 1995 in a shallow (<600 m) oil field located in Clinton County, Kentucky. Preliminary results of the first two tests revealed low-angle reservoir fractures that were not previously known to exist (Rutledge et al., 1994b). New data and further evaluation of the old data indicate both temporal and spatial relationships between the microseismicity and production.

Background

Potential for high-volume oil production has been demonstrated from shallow oil reservoirs in Clinton County, Kentucky (Figure 1) (Hamilton-Smith et al., 1990). Oil is produced from low porosity (<2%) carbonate rocks of Ordovician age, spanning the section from the Lexington Limestone to the Knox Group, at depths <600 m (Figure 2). Comparted fracture storage and permeability is suggested by isolated, high-volume production wells. Initial production rates as high as 64 m^3 per hour and cumulative production of 16000 m^3 from a single well have been reported. Sixty-five km west of Clinton County, near Glasgow, Kentucky, narrow trends of synclinal oil production from shallow (135 to 180 m) carbonate rocks have been associated with basement-controlled fault structures (Black, 1986a) (Figure 1). The Glasgow reservoirs are restricted to local zones of fractured, dolomitized limestones, interpreted to be related to secondary faults and fractures, resulting from right-lateral, strike-slip reactivation of a deeper basement fault. Similar basement-controlled Paleozoic structures and associated dolomitization have been

-3-

identified throughout central Kentucky (Black, 1986b). To our knowledge, no detailed investigations of the reservoir fracture systems have been conducted that would provide further guidance in exploration and field development in central Kentucky.

Our study area comprises a narrow trend of new production along the Indian Creek syncline extending about 2 km ENE from the Seventy-Six oil field (Figure 1). The Seventy-Six field was developed and abandoned in the late-1940s (Wood, 1948). Production resumed December, 1992 with the completion of the Petro-Hunt # 1 Frank Summers well on the eastern margin of the abandoned field (well FS1 of Figure 1). Microearthquakes were detected using downhole geophone tools placed at or near reservoir depth in wells located 120 to 250 m from new, high-volume wells. Typical high-volume wells in the study area flow oil to surface for a few days at rates of 80 to 240 m^3 per day and are then produced using sucker-rod pumps. Single-well, cumulative production is on the order of 1600 to 2400 m^3 over periods of 6 to 12 months. Production along the Indian Creek syncline has been primarily from the middle-Ordovician High Bridge Group (equivalent to the Stones River Group of Tennessee) at depths ranging from about 300 to 460 m (Figure 2). The High Bridge Group consists mainly of argillaceous limestone deposited in a shallow-marine to tidal-flat environment (Gooding et al., 1988).

Data

Data were collected using downhole, 3-component geophone tools. A mechanical arm couples the instruments to the borehole wall. The tools were equipped with 8 or 30 Hz geophones. Downhole amplification of the geophone outputs was 60 dB. At the surface the data signals are further amplified and anti-alias filtered before input to a triggered, digital data-acquisition system. Data were sampled at a 0.2 msec interval per channel.

The three microseismic monitoring tests were conducted sequentially, each near new, relatively high-volume production wells. No injection activity was conducted before or during monitoring. The associated production wells and sequence of monitoring was 1) the Petro-Hunt #1 Frank Summers (FS1); 2) the Meridian #1503 Frank Summers (FS2); and 3) the Ohio Kentucky Oil Corporation #1 Hank Thomas (HT1) (Figure 1 and Table 1). We use the associated high-volume production wells in referring to each monitor test.

Table 1 summarizes the monitor periods, geophone stations and number of microearthquakes detected during each test. Only one geophone tool was deployed during the FS1 test. The FS2 and HT1 tests each had two geophones placed 183 m apart within a single monitor well. For the HT1 test, a third geophone tool was deployed in a second monitor well 9 weeks after monitoring began (Table 1 and Figure 1). A 1-Hz, L-4 Mark Products geophone was also buried in a shallow hole (0.3 m) near monitor well M during the FS2 monitoring test. No microearthquake signals were detected on the surface geophone. An example of an event's 3-component waveforms from a single downhole tool is shown in Figure 3.

Monitor Site (production well)	Number of Events Detected	Monitor Period (m/d/y)	Total Monitor Period (weeks)	Downhole Geophone Stations (well: depth)		
FS1	110	2/5/93 - 4/12/93	$9^1/2$	M: 335 m		
FS2	180	9/17/93 - 2/8/94	$20^1/2$	M: 335 m	M: 152 m	
HT1	3237	1/8/95 - 8/5/95	30	GT8: 427 m	GT8: 244 m	BU1: 396 m

Table 1: Summary of events detected, monitor periods and geophone stations.

Gross production and event rates for the three monitor tests correlate, with changes in event rates lagging production rate changes by 2 to 3 weeks (Figure 4). The production curves shown for FS2 and HT1 include small contributions from other producing wells (<5% of total production) in the respective study areas. Cumulative seismic moment for the FS2 and HT1 data sets are also shown (Figures 4b and 4c). We were able to obtain moment measurements for 78% of the events comprising each of these data sets using low-frequency spectral amplitudes (Brune, 1970, equation 27). Moment-derived magnitudes (Hanks and Kanamori, 1979) range from -2.5 to 0.9 with a median of -1.0.

FS1 produced 762 m^3 of oil by natural flow in the first 9 days following drilling (Figure 4a). The well was then shut in for completion. Microseismic monitoring started week 8. Production resumed week 9. The event rate increased during week 11, about $2^1/2$ weeks after production resumed. Event and production rates were fairly constant for the remainder of the FS1 test (Figure 4a).

Monitoring of FS2 started $4^1/2$ weeks after initial production (Figure 4b). The production rate decline at week 6 has no corresponding decline in event rate. Pump rate was increased at week $11^1/2$ and is followed by an increase in event rate at week $14^1/2$. Production decline at week 15 also has no correlation to event rates, but the further decline in production at week 19 is followed by a decrease in event rate at week 21 (Figure 4b).

The highest rates of seismicity and the strongest correlation of seismic activity with production were associated with the HT1 test (Figure 4c). Monitoring of HT1 began 6 weeks after initial production. The decrease in production rate at week 13 is followed by a decrease in event rate at week 15. Production records for HT1 after week 22 are not available. We presume production continued to decline from week 22 to 28. HT1 production was terminated during week 28 when the well was deepened using an air-rotary rig. Deepening of HT1 directly connected the original productive interval with a water-filled (brine) fracture (located with production induced seismicity and discussed further below). HT1 was then plugged back to its original total depth (TD) and put back on-line. Production efforts were immediately terminated due to large volumes of water produced from the original production depth which had produced no water before deepening (L. Wagoner, Ohio Kentucky Oil Corp., pers. commun., 1995). The presence of water indicated the previously produced interval was at least partially repressurized via the borehole connection to the deeper fracture. A nearby lightning strike temporarily terminated monitoring beginning week 28, a few days before HT1 was deepened. Monitoring resumed from weeks $\sim30^1/2$ to 36 during which only 2 microearthquakes were detected (not shown in Figure 4c). In the 3 weeks before the HT1 productive interval was inadvertently repressurized, the event rate was 120 times greater than measured during the subsequent $5^1/2$-week monitor period.

The correlation of the production and event rates suggests the observed microearthquakes are triggered by production induced stress changes. The cumulative number of events detected and the total seismic moment at the HT1 site were 18 and 37 times greater, respectively, than observed at site FS2, though comparable volumes were extracted from both locations (Figure 4). After presenting an interpretation of the data, we will offer some speculation on the cause/effect relationships, the 2 to 3 week lag time between production and seismicity rates and the large difference in cumulative seismic moment released at sites HT1 and FS2.

Locating the Microearthquakes

Unique locations were determined for the multiple-tool deployments (FS2 and HT1 monitor sites). A combination of P- and S-wave arrival times and P-wave particle motion trajectories (hodograms) were used to obtain locations since these data were collected using only two to three receivers. Arrival times were picked visually and, in general, were very impulsive (Figure 3). Estimated errors in the arrival-time picks were 0.3 msec or less. Azimuthal hodogram data were determined by finding the principal eigenvector of the 2-dimensional covariance matrix for the first 2 msec of P-wave, horizontal-component data (Flinn, 1965). Criteria constraining the quality and use of the directional data (hodograms) were first-arrival signal-to-noise ratio ($\geq$10) and linearity of particle motion (Rutledge et al., 1994b). Velocities were initially determined using sonic logs, downhole calibration shots, and finally, using a joint hypocenter-velocity inversion. The downhole calibration shots were also used for determining the orientation of the geophone tools' horizontal components.

Two-station data, in which two receivers were placed in a single borehole 183 m apart, make up the entire FS2 data set and the initial 59% of the data collected at the HT1 site. Two-station hypocenters were determined in two separate steps, first using the traveltime data to obtain a depth and radial distance from the monitor well, and then using the hodogram data to obtain a unique azimuth to the source (Rutledge et al., 1994b).

In computing the HT1 hypocenters for events recorded on three stations, traveltime and hodogram data were coupled in an iterative, least-squares computation minimizing the difference between predicted and observed data (Phillips et al., 1998). Azimuthal hodogram data from the station in BU1 and the lower station in GT8 were used (Table 1). These stations had higher signal-to-noise ratios and shorter, lower inclination receiver-source paths than the upper station in GT8. Scaling of traveltimes and angles in units of length was applied to avoid numerical problems with matrix elements differing by orders of magnitude. Data were weighted by the reciprocals of their uncertainties, estimated from residuals of the three-station data (Table 2). Location errors are discussed below.

A velocity model was calibrated using downhole shots and a subset of the HT1 three-station data via a joint hypocenter-velocity inversion. These data included P-wave arrival times and hodograms from three downhole shots and 364 events in which six arrival times (three P and three

Station Well: Depth (m)	P Arrival (msec)	S Arrival (msec)	Hodogram Azimuth (Degrees)
GT8: 244	0.5	0.1	(not used)
GT8: 427	0.3	0.1	5
BU1: 396	0.3	0.1	4

Table 2: Residual standard deviation of the HT1 three-station data.

S) and two hodograms were available. We solved for a two-layer velocity model, event locations and the two deep geophone orientations (BU1 and lower GT8 receivers, Table 1). Parameter separation techniques were used allowing an unlimited number of events to be included in the inversion (Pavlis and Booker, 1980). The boundary between the two layers was kept fixed at the well-defined sonic-velocity boundary at the top of the High Bridge Group (Figure 2). Inclusion of the hodogram data helped resolve the trade-off between velocities and hypocenters. In general, the hypocenters aligned in distinct planar clusters (presented below). The final velocity model was considered improved from the starting model based on better coplanar alignment of two- and three-station data hypocenters.

Microseismic Fracture Maps

Of the 180 events identified during the FS2 monitor test, 165 had clear P- and S-wave arrivals that could be identified on both receivers, and, of these, 121 could be located. A map view is shown in Figure 5 and a cross-section projection of hypocenters along profile A-B of the map view is shown in Figure 6. A perspective view of fractures defined by four planar, hypocenter clusters is shown in Figure 7. The strike and dip of these planes are given in Table 3.

FS2 Hypocenter Groups	Strike	Dip	Composite Focal Mechanism Nearest Nodal Plane		
			Strike	Dip	Rake
◆ Group 1	N65°E	24° NW	N92°E ±5°	22° NW ±5°	116° ±20°
▼ Group 2	N61°E	27° NW			
● Group 3	N64°E	34° SE	N90°E ±10°	45° SE ±15°	110° ±10°
■ Group 4	N68°E	20° SE			

Table 3: Orientations of FS2 hypocenter groups and nearest nodal plane. Rake of 0° = left lateral displacement, 90° = reverse (thrust), ±180° = right lateral, -90° = normal.

For the HT1 microseismic data, 1719 of the 3237 events detected were located. A map view is shown in Figure 8. The majority of events (1548) are located east of well GT3. A cross-section projection of the events located east of GT3 along the profile line C-D of the map view (Figure 8) is shown in Figure 9. A perspective view of three fracture planes delineated east of GT3 is shown in Figure 10. Orientations of these planes are very similar to the fractures delineated near FS2 (Tables 3 and 4).

HT1 Hypocenter Groups	Strike	Dip	Composite Focal Mechanism Nearest Nodal Plane		
			Strike	Dip	Rake
Group A	N65°E	19° NW	N47°E ±5°	27° NW ±5°	70° ±20°
Group B	N82°E	17° SE	N80°E ±35°	20° SE ±10°	90° ±40°
Group C	N67°E	16° SE			

Table 4: Orientations of HT1 hypocenter groups and nearest nodal plane. Rake of 0° = left lateral displacement, 90° = reverse (thrust), ±180° = right lateral, -90° = normal.

Except for the group C plane (Figure 10), grouping the hypocenters into planar clusters was accomplished by visual inspection using various 2-dimensional projections and 3-dimensional graphic displays. The planar volumes shown in Figures 7 and 10 were then determined from the eigenvectors of the covariance matrix of the 3-dimensional microearthquake locations within each group (Flinn, 1965). The strike and dip of the planes listed in Tables 3 and 4 were determined from the minimum eigenvectors (normals to the planes).

A hint of the group C events can be seen in the projection of Figure 9, dipping to the SE, but it is partially obscured by the events of larger group A. Group C was defined by a set of unique waveforms in which the S-waves observed on the upper geophone in GT8 were nodal (e.g. Figure 11). Comparison and grouping of waveforms, based on S to P amplitude ratios and location constraints, has been used to identify planes within irregular volumes of seismicity (Roff et al., 1996). The identification of the group C plane (Figure 10) is a simple example of this technique. The waveforms observed on the upper geophone in GT8 are easily distinguished by the high amplitude P-wave and nearly nodal S-wave arrivals (e.g. Figure 11). Two hundred seven of these waveforms were identified and were found to define an elongate plane beneath, and intersecting the northern edge of the larger, opposite-dipping, group A cluster (Figure 10). The very distinct seismicity boundary immediately south of GT8 is formed by this intersection (Figure 8)

<u>Location errors</u>

Uncertainties for both the FS2 and HT1 data were estimated from residuals of the HT1, three-station data (Table 2). These errors only reflect the station-event geometry, the distribution of data types, and data uncertainties; velocity model uncertainties were not considered. Error ellipses in general are linear and trend perpendicular to the event-station direction due to the larger error contribution associated with the hodogram azimuths (Table 2). Error in depth and radial distance from the monitor boreholes are predominantly associated with the arrival time uncertainties (solely for the two-station locations) and, hence, are smaller. For the two-station event location the maximum axis of the error ellipsoids are horizontal and ranged between 10 and 20 m within 250 m of the monitor boreholes, and up to 75 m for the most distant events (850 m).The location errors for the HT1 three-station data east of GT3 (Figures 8 and 9) range between 3 and 5 m. Events that lie close to the N-S plane through the two monitor boreholes (GT8 and BU1) have errors up to 20 m and ellipses that are highly linear, trending E-W. Well-log porosity anomalies corroborate the intersection of the seismically-active fractures at wellbores (presented below). Accuracy of the intersection of the group-computed planes, defined by the maximum and intermediate eigenvectors, with the log anomalies ranges from 0.5 to 3 m within 250 m of the monitor wells.

Fault Plane Solutions and State of Stress

Composite fault plane solutions were computed for the planar hypocenter groups using the computer program FPFIT (Reasenberg and Oppenheimer, 1985). Figure 12 shows the best fit fault plane solutions for the FS2 and HT1 groups identified in Figures 7 and 10. Convergence to a single solution was achieved in each case. First motion data from all receiver tools were used. Horizontal component first motions were used, after correcting for tool orientation, from the deeper geophone tools with lower inclination source-receiver paths. Hypocenter planes with the same direction of dip were combined to improve the focal sphere coverage. Discrepant first motions were few ($\leq$ 9%) except for the HT1 group A plane (22%). However, most of the HT1 group A discrepants are associated with the GT8 upper-geophone-tool first motions which straddle one of the nodal planes where uncertainty in polarity would be greatest (Figure 12c). All four composite fault plane solutions indicate a predominantly thrust mechanism. P axes are consistently oriented NW-SE at near-horizontal inclination. Uncertainty within the 90% confidence limit are shown for P and T axes (Figure 12) and listed for the nodal plane closest to the mapped fault planes (Tables 3 and 4)

-10-

(Reasenberg and Oppenheimer, 1985).

The four composite focal mechanisms are consistent and show fairly good agreement of a nodal plane orientation with the hypocenter-determined planes (Figure 12 and Tables 3 and 4). This suggests that the assumption of common mechanisms occurring along similarly-oriented rupture surfaces within the mapped planes is good. The median area of rupture surfaces for individual events is only about 50 m^2 (Schuessler et al., 1995), whereas the larger hypocenter-defined planes have areas up to 3.5 x 10^5 m^2. S-P amplitude ratios are also consistent with coplanar orientation of the individual rupture surfaces and the larger, mapped planes. As an example, the first motions for the group C plane recorded on the GT8 upper receiver are centered in the compressive quadrant of Figure 12d, where, as observed (Figure 11), the P- and S-wave amplitudes should be anti-nodal and nodal, respectively (Aki and Richards, 1980, p. 82). The dip of the group C plane is within 8° of the theoretical orientation at which this amplitude relationship would be observed at the GT8 upper receiver for pure reverse-slip motion at the plane centroid. Our observations indicate uniform sense of motion, preferentially along similarly-oriented, low-angle faults. This is in contrast to highly variable focal mechanisms observed during large hydraulic fracture operations (e.g. House and Jensen, 1987; Cornet and Jianmin, 1995; House et al., 1996). Presumably this uniform seismic slip is controlled by the background state of stress.

Stress

Principle stress orientations and relative magnitudes were computed using Gephart's (1990) focal mechanism stress inversion computer program (FMSI) which implements the method of Gephart and Forsyth (1984). The four composite focal mechanisms are the minimum amount of data required to implement this procedure. Input data were the nodal plane orientations with the fault planes identified, in all four cases, as the nodal plane closest to the mapped planes. Knowledge of the correct fault planes helped constrain the solutions. The exact method of finding the best stress model was conducted using a grid search over the entire lower hemisphere at 5° increments (Gephart and Forsyth, 1984). Resultant principle stress orientations are shown in Figure 13 within the 95% confidence limit. Average angular rotation required to bring the observed fault planes and slip direction into agreement with the final model (within the 95% confidence limit) is <5°. Maximum principle stress, σ_1, is near horizontal, trending N15°W ±15°. The small

number of focal mechanisms and the similar orientations of active faults observed leave the σ_2 and σ_3 orientations more poorly resolved (Figure 13). Correspondingly, the relative stress magnitude R (where $R = (\sigma_2 - \sigma_1)/(\sigma_3 - \sigma_1)$) was poorly resolved, ranging from 0.65 to 0.95 within the 95% confidence limit.

Relatively high compressive stress at the shallow depths (<550 m) of the study area is indicated by the thrust type fault-plane solutions and the stress inversion. Evans (1989) has shown a near-surface (<600 m) thrust stress regime to be ubiquitous throughout the Appalachian Basin from eastern Kentucky to western New York. Our data indicate that this same near-surface stress regime persists further south and west. Orientation of maximum horizontal stress (S_H) at our shallow depth of measurements ($S_H=\sigma_1$) is rotated approximately 90° from the regional direction. S_H is consistently oriented ENE-WSW from the U.S. midcontinent region, west of our study area, to the eastern side of the Appalachians (Zoback and Zoback, 1980; Evans, 1989; Zoback, 1992). More specifically, in central Kentucky S_H direction would be expected to be between values measured in eastern (N51°E) and western (N81°W) Kentucky (Plumb and Cox, 1987). The rotation of S_H from expected regional orientation may be due to local structural control. Further, this anomalous stress orientation may only exist at shallow depth due to variation in principle horizontal stress gradients at the near surface, resulting in S_H and S_h being flipped with respect to orientation at greater depth (S_h=minimum horizontal stress).

Interpretation

At both production sites along the Indian Creek syncline, the microearthquakes have revealed sets of low-angle thrust faults within and immediately above the High Bridge formation. These thrust faults strike about N65°E and dip to both the NW and SE at angles ranging from approximately 15° to 35° (Tables 3 and 4). Below, we summarize the relationship of the seismically-active fractures with respect to production, local geology and inferred pressure history.

Seismically-Active Fractures and Production

The seismically-active fractures occur away from or outside of currently-drained depth intervals. While monitoring FS2, 95% of the fluid volume extracted in the immediate area was

produced from FS2 (about 1750 m^3). Well FS1 was intermittently on-line during the FS2 monitor period and contributed about 2% (40 m^3) of the oil production plus some small volume of water (water volume records were not kept). The other 3% (48 m^3) came from well PD1 during the last 5 weeks of monitoring (Figures 5, 6 and 7). Along the strike direction of the mapped planes, the production-depth interval of FS2 projects close to the two minor fractures delineated by hypocenters groups 2 and 4 (Figure 6), but is located east of these fractures as seen in map and perspective views (Figures 5 and 7, respectively). The largest seismically-active fracture (group 1) is clearly outside of the production depth intervals of FS2 and FS1 (Figures 6 and 7).

A similar relationship was observed during monitoring of HT1; 97% of the fluid volume extracted during monitoring was produced from HT1 (> 1300 m^3). The seismicity occurs both above and below the production interval of HT1 (Figures 9 and 10) and, in map view, primarily to the west of HT1 (Figure 8).

The seismically-active fractures have been partially drained by previous production and have subsequently been resaturated with brine (water). Three of the fractures mapped on the Summers lease are intersected by the monitor well M (hypocenter groups 1, 2 and 4 of Figure 7). Well M is an old production well drilled in the late 1940's, identified as the Summers #3 well in Wood (1948), and is currently water-filled, uncased and obstructed at 378 m. The original TD of M was 489 m which puts the well termination at the base of the major fracture defined by hypocenter group 1 (Figures 6 and 7). When drilled, cable-tool drilling was used in the area. Like air-rotary drilling, cable-tool drilling is typically terminated when substantial fluid flow is encountered. There are no records of the depth intervals produced or volumes extracted from well M, but it is likely that the group 1 fracture intersected at the original TD was at least partially drained by M in the late 1940's. Whether group 2 and 4 fractures were originally water or oil filled, they would have undergone some drainage during drilling. The intersection of the group 2 fracture at about 267 m depth is corroborated with a density-derived porosity anomaly from 267 to 269 m. (The density-log interval was terminated above the group 4 fracture intersecting well M at about 366 m depth.) Since well M is open to formation and water filled, the three fractures intersecting the well should be at hydrostatic pressure. The group 1 plane was intersected by well GM3, drilled subsequent to monitoring, in April, 1995. Brine was encountered at 313 m where GM3 intersects the group 1 plane (Figures 5, 6 and 7).

At the HT1 site the seismically-active fractures and production history show a similar relationship. In map view the main seismic zone is bounded by older production wells, GT1, GT2, GT3 and GT4 (Figure 8). Production depth intervals of GT1, GT2 and GT4 intersect or align with the seismically-active fractures (Figures 9 and 10). GT4's production interval intersects the up-dip side of the A fracture. GT2's upper production interval intersects the B fracture and its lower production interval, brought on-line after deepening the well, aligns with the C fracture. The productive interval of GT1 aligns with the A fracture's down-dip side (Figures 9 and 10). When deepened, GT2 also intersected the up-dip side of the A fracture and is correlated with temperature- and neutron-porosity log anomalies. GT2 did not produce oil from the A fracture, most likely because of partial drainage already underway from GT1 and GT4. A cumulative oil volume of 725 m^3 was extracted from these 3 wells in the 9 months proceeding monitoring. Only GT1 was on-line with HT1 during monitoring, and it only contributed an additional 25 m^3 of oil. Small volumes of water (brine) were also produced from GT1, GT2 and GT4 (water production records were not kept). HT1 produced no water (L. Wagoner, Ohio Kentucky Oil Corp., pers. commun., 1995).

A test well, GT10, was drilled by the Ohio Kentucky Oil Corporation (OKOC) into the lower edge of the group A fracture after 5 months of monitoring. No fluid was encountered until the drill bit reached the group A fracture at 432 m (Figures 8, 9 and 10). The fracture produced brine with drill-string air circulation (air rotary drilling) and drilling was immediately terminated. One week later, OKOC deepened HT1 and also encountered brine when the well intersected the same group A fracture further up dip at 404 m (Figures 9 and 10). Below, we discuss the source of the brine.

Production wells PD1, IW2, IW4 and MF2 (Figures 5, 6, and 7) are located about halfway between the FS2 and HT1 monitor sites. These four wells are also shown unmarked in Figure 14 in between the FS2 and HT1 hypocenters. A cumulative 719 m^3 of oil was extracted from PD1, IW2 and IW4. MF2 was a potential producer but was never put on-line due to well completion problems. Ninety-one percent of the oil (654 m^3) was produced during the 11-month gap between the FS2 and HT1 geophone deployments (Table 1). Production from PD1 spanned both tests contributing only 48 m^3 during FS2 monitoring and 17 m^3 during HT1 monitoring. Along the strike direction of the active fractures, production-depth intervals of PD1, IW2 and IW4 project on or close to the group 1 fracture (Figures 6 and 7). The HT1 group A cluster aligns at depth with group 1 when plotted with respect to the same elevation and is probably extension of the same

structure. The extent of east-west permeability continuity along the group 1 - group A fault is unknown.

Along the Indian Creek syncline, the oil reservoir in the High Bridge Group is primarily a set of comparted, low-angle thrust faults. This conclusion follows from the correlation of the older production depth intervals and the mapped, low-angle thrust faults. Logged boreholes intersecting the seismically-active fractures show distinct porosity-log anomalies (density, neutron and/or temperature) over 1 to 2 m intervals. Density-neutron porosity logs are shown in Figure 15 for the seismically-active productive interval of GT1 and the seismically-inactive productive interval of HT1. These are examples in which the boreholes were not enlarged or irregular over the fractured, productive zones, allowing reliable log-porosity estimates to be obtained. Over the intervals where the density-derived porosity exceeds the neutron porosity (the gas-crossover effect), maximum porosity is estimated as the root-mean-square (rms) of the two peak log values (Asquith, 1982, p. 68). Using the log values averaged over 1 m of the highest porosity intervals exhibiting crossover as inputs to the rms computation, gives a 7% average porosity for both the GT1 and HT1 productive zones. The 1 m thickness associated with the average porosity estimates can only be considered a maximum thickness of the porous, fracture intervals since the displayed logs represents data smoothed or averaged over larger depth intervals. From these values, we can roughly estimate an upper limit of a mapped fracture's pore volume.

For the group A fracture we estimated pore volume using the surface area delineated by the microseismicity and fracture-zone thickness and porosity estimated from the GT1 log data. The active area of the fracture mapped east of GT3 is approximately 300 by 100 m. Using the well-log estimate of 7% porosity developed over a 1 m interval gives a total pore volume of 2100 m^3. Productive intervals of GT1 and GT4, which align with the group A fracture zone, produced a cumulative 402 m^3 of oil or 19% of the fracture's computed pore volume.

The correlation of the event rates and HT1 production suggests that the microseismicity is triggered by the current-production induced stress changes (Figure 4c). The spatial correlation of the microseismicity to past production in turn suggests that current drainage follows a similar pattern. Based on these inferences and the similarity of the log responses (Figure 15), we presume that HT1 also produces from a low-angle fracture oriented similar to the adjacent, seismically-active fractures. A plane formed by the productive intervals of HT1, GT3 and a weak temperature

anomaly in GT10, at 354 m, strikes N72°E and dips 22° SE, consistent with the mapped thrust-faults (Tables 3 and 4 and Figure 10). GT3 was the second, single largest producer in the HT1 monitor area (544 m^3) and also produced at a depth interval between the seismically-active fractures. The inferred fracture would have been partially drained by GT3 before HT1 was drilled and intersected it further down dip (Figure 10). Initial production response supports this interpretation. GT3 initially flowed oil to surface, HT1 did not. Test well GT10 aligns closest with HT1 and GT3 along strike of the microseismic mapped structures, and its temperature anomaly gives the third point defining the plane. The GT10 log showed no other significant anomalies (the group A fracture intersected at TD could not be spanned by the logging tool). There are no log anomalies indicating the inferred fracture intersects the surrounding production wells GT1, GT2 and GT4. Production history also indicates these wells have very poor or no hydraulic conductivity with the volume drained by HT1. Permeability and porosity of the inferred fracture, therefore, are developed over a narrow zone in the dip direction (<60 m at S18°E). The narrow zone of seismicity extends about 850 m SW of HT1 (Figure 8) suggesting an extensive pressure response in the strike direction. Evidence of immediate pressure communication between wells has been observed in the area at distances greater than 1 km and has been interpreted as intersection with a common fracture (J.H. Perkins, Petro-Hunt, Inc., pers. commun., 1996).

Local Geologic Structure

Historical displacements along the imaged thrust faults are small with vertical throws of about 1 m or less (Hamilton-Smith, 1995). Detailed log correlations show about 1 m of thickening in section just above the group 2 mapped thrust fault (Figure 7). The observed thickening could also be due to local infill sedimentation. We can conclude that total historical displacements in dip direction do not exceed about 2 m.

The east-west trending Indian Creek syncline is a very low-relief structure mapped predominantly from Mississippian outcrops (Lewis and Thaden, 1962, 1965). Local subsurface expression of the structure at the top of the High Bridge Group is shown in Figure 1 and again in Figure 14 with the FS2 and HT1 microearthquake locations. The surface structure is clearly associated with a basement graben seen on a reflection seismic profile crossing the Indian Creek syncline near wells FS1 and FS2 (S.K. Jones, Meridian Exploration Corp., pers. commun., 1995). The structural low propagates upward with diminished relief and depositional infilling suggesting

episodic, Paleozoic reactivation of the basement structure (Hamilton-Smith, 1995). Basement-controlled wrench faults have been associated with synclinal oil production from shallow, fractured, Ordovician carbonates 65 km west of Clinton County (Black, 1986a). Recent drilling programs along the Indian Creek syncline have been based on a similar interpretation of fracture/lineament patterns delineated on side-looking airborne radar images. Features associated with these structures are secondary faults and fold axes lying en echelon along the main, underlying fault, formed by strike-slip displacement of the deeper fault (Harding, 1974). In Kentucky, only near vertical fracture sets have been considered in the wrench-fault interpretations, although en echelon thrust faults should also be expected with convergent, strike-slip movement (Harding, 1974). The significant result of the microseismic monitoring has been the identification of the small-displacement thrust faults and their association with oil production. Though previously unidentified, these structures, lying along and striking oblique (~N65°E) to the east-west trending Indian Creek syncline (Figure 14), are consistent with Hamilton-Smith's (1995) and local operators' right-lateral, wrench-fault interpretations.

Pressure History

In this section we attempt to describe the reservoir pressure history and estimate pressure changes that may be inducing the observed microseismicity. In the absence of known reservoir pressure measurements, we base this description on some simple assumptions and field observations that at least allow us to arrive at reasonable limits of reservoir pressure changes.

Initial production in the study area is characterized by high-volume flow to the surface. Wells are typically put on pump within a few days of discovery as pressure declines. Based on high-volume flow to surface, it has been suggested that the reservoirs are initially overpressured (Hamilton-Smith, et al., 1990; Hamilton-Smith, 1995). Hydrostatic head alone, however, can account for the observed flow. Well FS1, for example, flowed 236 m^3 to a tank battery elevated about 12 meters above the wellhead within the first 24 hours of production. Water levels measured in static wells open to reservoir depth correspond to 3 m below the FS1 wellhead. This could support a column of oil in FS1 from the production depth at 305 m to 63 m above the wellhead (oil density = 0.82 g/cm^3 (Hamilton-Smith, 1995)). Brine in the geologic section and gas in the oil would increase the oil's buoyancy.

The drained fractures eventually recover to hydrostatic pressure via brine invasion as indicated by fluid levels in wells intersecting the seismically-active fractures. Water levels in well M (Figures 6 and 7) were repeatedly measured at 13 m depth (247 m elevation) throughout monitoring. Well GT2 connects with the seismically-active fractures at the HT1 site (Figures 9 and 10) and was also water-filled to the near surface during monitoring (37 m depth, 249 m elevation). If the reservoir is initially overpressured it implies that a net pore-pressure decrease occurs along fractures from pre-drainage to subsequent hydrostatic recovery, which would inhibit seismic slip. Therefore, the observed seismic failure along the pressure-cycled fractures suggests the reservoir cannot be overpressured. We assume instead that the reservoirs are initially in equilibrium with far-field pore pressure (hydrostatic) so that little or no net pressure change results from the pressure cycling. In fact, a small pressure increase should occur along the pressure-cycled fractures as a result of produced oil being replaced with denser brine (discussed further below).

The evidence of brine invasion along the previously productive fractures with eventual hydrostatic pressure recovery suggests a natural water drive is active in the area. However, the water drive is very poorly connected to the productive fractures via natural reservoir flow paths and is unable to maintain reservoir pressure during drainage. Pressure decline is evident by the short duration of flow to the surface. Hydraulic isolation of the productive fractures is evident from very low to nonexistent water (brine) production during the wells' short productive histories and the highly comparted nature of production from adjacent, sequentially drilled wells. Brine invasion and pressure recovery of the drained fractures is often facilitated by open-well completions, allowing direct communication between permeable zones at different depths.

An upper limit of reservoir pressure decline would be due to complete removal of fluid from the production well by pumping. This limit is reasonable because as pressure declines, pump capacity can surpass inflow to the wells. Pumping is then cycled allowing intermittent, partial fluid-level recovery in the well. Assuming the reservoir was initially at hydrostatic pressure, emptying the well is equivalent to a pressure drop (Δp) by removal of about 300 m of brine. Using an assumed density of sea water (ρ=1.03 gm/cm^3) Δp = -3 MPa. Pressure reduction away from the borehole would be less.

Production-Induced Stress Change

We consider two possible mechanisms by which production may be promoting the observed seismic slip: 1) increased horizontal compression above and below currently drained volumes due to poroelastic effects, and 2) reduction of effective normal stress across previously productive fractures due to brine replacing oil.

Poroelastic stresses will be generated outside a drained volume due to contraction of the reservoir rock accompanying production (e.g. Segall, 1989). The magnitude of horizontal stress change $\Delta\sigma_h$ centered just above or below an axisymmetric, flat-lying ellipsoidal volume undergoing uniform pressure change Δp is given by $\Delta\sigma_h = -\alpha\Delta p\left(\frac{1-2\upsilon}{1-\upsilon}\right)\frac{\pi}{4}\frac{a_3}{a_1}$ where α is the Biot coefficient, υ is Poisson's ratio and a_1 and a_3 are the reservoir semi-major axes in horizontal and vertical directions, respectively (Segall and Fitzgerald, 1998). Compressive stress is positive. At the HT1 site $a_3/a_1 = 0.5 \text{ m}/30 \text{ m} = 0.017$ corresponding to the inferred, drained fracture dimensions in the σ_3-σ_1 plane (a_3 from HT1 well log, Figure 15, and a_1 from the length along dip direction, Figure 10). $\alpha = 0.43$ was determined using a log-derived porosity of 7% and an empirical curve of α versus porosity for carbonate rocks (Laurent et al., 1990) as summarized by Segall et al. (1994). $\upsilon = 0.36$ was determined from the seismic velocities (Figure 2). Using these parameters and a pressure drop <3 MPa, $\Delta\sigma_h$ outside the currently-drained volume at the HT1 site is <0.008 MPa.

Pressure re-equilibration of the previously productive fractures by replacement of oil with denser brine will result in a small pore pressure increase relative to pre-drained pressure, thereby decreasing effective normal stress across the fracture. Uniform drainage and brine replacement along the fractures will result in a pressure increase $\Delta p = \Delta V \Delta\rho g h$ where ΔV is the portion of pore volume produced as oil, $\Delta\rho$ is the density difference of brine and oil, g is gravitational acceleration and h is the height of the fracture due to its dip. For the group A fracture, (Figures 9 and 10), ΔV = 19% (presented above), $\Delta\rho = (1.03 - 0.82) = 0.21 \text{ gm/cm}^3$, and h = 35 m maximum, giving a maximum $\Delta p = 0.014$ MPa along the deepest portion of the seismically-active fracture.

Discussion

Both triggering mechanisms seem plausible in light of the spatial and temporal relationships observed between production and seismicity. The temporal correlations (Figure 4) suggests the seismicity is triggered by current-production induced stress changes, and the spatial occurrence of the seismicity is similar to that expected for Segall's (1989) poroelastic model of extraction-induced stress changes for relatively flat-lying drainage volumes. Consistent with the model, slip is inhibited along the currently-drained fracture (e.g. the inferred, aseismic fracture shown in Figure 10) because the effective stress loading predominantly increases the normal stress across the fracture; reverse slip is triggered on fractures above and below the drained volume (e.g. fractures A, B and C of Figure 10) due to small increases in horizontal compression induced by production. As is our case, reverse faulting triggered above or below the reservoir by poroelastic compression would only be expected within a thrust stress regime because the stress changes are so small (Segall, 1992; Segall et al., 1994; Segall and Fitzgerald, 1998). In addition, the occurrence of seismicity along the surrounding, pre-drained fractures also suggests that the mechanism of pore pressure increase, or reducing effective normal stress via brine invasion, may itself be triggering shear slip or at least driving the pressure-cycled fractures closer to shear failure.

Magnitude of total estimated stress change promoting slip is about 0.02 MPa. Correlations of increased aftershock activity occurring in regions where computed, mainshock-induced static stress has also increased, suggests earthquakes can be triggered by stress changes as small as 0.01 to 0.05 MPa (Reasenberg and Simpson, 1992; Stein et al., 1992). Our estimated limit of poroelastic stress change outside currently-drained volumes (<0.008 MPa) is approaching magnitudes of tidal-induced stress change (0.005 MPa, Stacey, 1969, p. 217) and may not be great enough alone to trigger slip. The relative importance of the poroelastic and oil-replacement stress changes depends on the log porosity estimates, though total stress change will not vary much within reasonable limits of porosity. If, for example, the logs used are not representative of the overall fracture porosity away from the boreholes, and fracture pore volume is actually larger than we estimated, then the poroelastic-induced compression increases and the pore-pressure change accompanying oil replacement becomes smaller. As in the studies cited above, the small stress changes associated with seismicity implies that the active fractures or faults are already critically stressed for shear failure within the background state of stress, and, in our case, further implies a correlation of critically stressed reservoir fractures with production (porosity and permeability anomalies). Seismicity triggered by small stress changes, in turn, should reflect the background state of stress,

exhibiting uniform focal mechanism on similarly oriented faults, consistent with what we have observed (Figure 12).

The discrepancy in number of events and total seismic moment observed at the FS2 and HT1 sites (Figure 4) may be due to the older production history near the FS2 site. Events rates during the FS1 test were comparable to the subsequent and adjacent FS2 test (Table 1 and Figure 4). Wells FS1 and FS2 are located on the margins of the older Seventy-Six oil field, developed and abandoned in the late 1940s (Figure 14). The most seismically-active fracture at the FS2 site (group 1, Figure 7) was probably productive 45 to 50 years ago, whereas, at the HT1 site, the seismically-active fractures were produced in the 7 months before HT1 came on-line. Release of additional strain energy at the FS1-FS2 production site could have occurred during the earlier production or more gradually over the intervening 45 to 50 years before production activity resumed.

Finally, we computed pressure response versus time at 150 m distance from a production well using Theis's (1935) solution for a confined aquifer (Freeze and Cherry, 1979, p. 317) to see if the response provided any insights to the 2 to 3 week delays observed between production and event rates. One-hundred-fifty meters corresponds to the horizontal distance from the HT1 well to the center of the most seismically-active fracture (group A, Figures 8, 9 and 10). Computed pressure decline and recovery magnitudes varied for a range of reasonable hydrogeologic properties, but the delay characteristics were similar in all cases. As shown in the example of Figure 16, the pressure response at 150 m is strongly affected almost immediately by step-rate changes in production. The response curves for pressure within the currently-drained fracture do not explain the observed delays unless some pressure thresholds controlling failure rate are crossed 2 to 3 weeks after production-rate changes. Determining what the pressure thresholds might be would require more accurate knowledge of the reservoir's hydrogeologic properties.

Conclusions

Mapping the production-induced microseismicity has revealed previously undetected, small-displacement, low-angle thrust faults. Correlation of these faults with older production intervals and well-log porosity anomalies indicates that these types of features should be considered potentially important drilling targets in the continued exploration and development of the area. The microseismicity only reveals those fractures or faults with a propensity to slip due to their orientation with respect to the current state of stress. Barton et al. (1995) have shown correlations

of much higher permeability along fractures oriented optimally for shear failure than fractures less critically stressed in current stress fields. Our study appears to further support those correlations. Surface lineament and outcrop studies indicate a complex variety of fracture sets in the region (e.g. Black, 1986b; Hamilton-Smith, 1995). Other fracture sets or faults present in the study area may play an important role in compartmentalizing the productive, low-angle faults.

The small-displacement thrust faults pose a difficult exploration problem using conventional seismic reflection data; they are too thin (<2 m) to be imaged directly and do not have enough vertical throw to resolve bedding discontinuities. Consideration of the low-angle fractures as exploration targets will probably require inference from other features such as the deeper, higher relief basement structures seen on reflection seismic data in the area. If the shallow thrust faults are indeed associated with a basement-controlled wrench structure, then they may be part of flower structures, steepening and converging with the main fault zone at greater depth (see Harding, 1990).

The identification of the productive, low-angle fractures also has implications for field development. Drilling horizontal or deviated wells at these shallow depths does not appear to offer any advantage in increasing the probability of intersecting productive fractures. Dip meter or formation microscanning logs would be useful in determining orientations of low-angle, productive fractures, enabling interwell correlation and mapping of pay zones, and further, provide guidance in offset well placement. Interwell correlation and mapping of the conductive fractures will also allow improved planning in plug-and-abandonment operations so as to avoid premature water invasion of pay zones. Pressure maintenance operations could also be attempted once the conductive fracture zones between wells have been mapped.

Acknowledgment

References

Albright, J.N. and Pearson, C.F., 1982. Acoustic emissions as a tool for hydraulic fracture location: experience at the Fenton Hill hot dry rock site. Soc. of Petro. Eng. J., 523-530.

Aki, K. and Richards, P.G., 1980. Quantitative seismology, theory and methods, volume 1. W.H. Freeman and Co., San Francisco.

Asquith, G. 1982, Basic well log analysis for geologist. Am. Assoc. Petro. Geologists, Tulsa, Oklahoma.

Barton, C.A., Zoback, M.D. and Moos, D., 1995. Fluid flow along potentially active faults in crystalline rock. Geology, 23, 683-686.

Batchelor, A.S., Baria, R. and Hearn, K., 1983. Monitoring the effects of hydraulic stimulation by microseismic event location, a case study. SPE paper 12109, presented at 58th Soc. Petro. Eng. Annual Technical Conference and Exhibition, San Francisco, California.

Black, D.F.B., 1986a. Oil in dolomitized limestone reservoirs in Kentucky. In: M.J. Aldrich, Jr. and A.W. Laughlin (Editors), Proceedings of the 6th International Conference on Basement Tectonics. Int. Basement Tectonics Assoc., Inc., Salt Lake City, Utah.

Black, D.F.B., 1986b. Basement faulting in Kentucky. In: M.J. Aldrich, Jr. and A.W. Laughlin (Editors), Proceedings of the 6th International Conference on Basement Tectonics. Int. Basement Tectonics Assoc., Inc., Salt Lake City, Utah.

Block, L.V., Cheng, C.H., Fehler, M.C. and Phillips, W.S., 1994. Seismic imaging using microearthquakes induced by hydraulic fracturing. Geophysics, 59, 102-112.

Brune, J., 1970. Tectonic stress and the spectra of seismic shear waves from earthquakes. J. Geophys. Res., 75, 4997-5009.

Cornet, F.H. and Jianmin, Y., 1995. Analysis of induced seismicity for stress field determination and pore pressure mapping. Pure Appl. Geophys., 145, 677-700.

Davis, S.D. and Pennington, W.D., 1989. Induced seismic deformation in the Cogdell oil field of west Texas. Bull. Seism. Soc. Am., 79, 1477-1494.

Deflandre, J.P., Laurent, J., Michon, D. and Blondin, E., 1995. Microseismic surveying and repeated VSPs for monitoring an underground gas storage reservoir using permanent geophones. First Break, 13, 129-138.

Doser, D.I., Baker, M.R. and Mason, D.B., 1991. Seismicity in the War-Wink gas field, Delaware Basin, Texas, and its relationship to petroleum production. Bull. Seism. Soc. Am., 81, 971-986.

Eberhart-Phillips, D. and Oppenheimer, D.H., 1984. Induced seismicity in The Geysers geothermal area, California. J. Geophys. Res., 89, 1191-1207.

Evans, K.F., 1989. Appalachian stress study 3. Regional scale stress variations and their relation to structure and contemporary tectonics. J. Geophys. Res., 94, 17619-17645.

Fehler, M., House L. and Kaieda, H., 1986. Seismic monitoring of hydraulic fracturing: Techniques for determining fluid flow paths and state of stress away from a wellbore. In: Proc. 27th U.S. Symposium on Rock Mechanics. Tuscaloosa, Alabama, June 23-25.

Flinn, E.A., 1965. Signal analysis using rectilinearity and direction of particle motion. Proc. I.E.E.E., 53, 1725-1743.

Freeze, R.A. and Cherry, J.A., 1979. Groundwater. Prentice-Hall, Inc., Englewood Cliffs, New Jersey.

Gephart, J.W., 1990. FMSI: A FORTRAN program for inverting fault/slickenslide and earthquake focal mechanism data to obtain regional stress tensor. Comput. Geosci., 16, 953-989.

Gephart, J.W. and Forsyth, D.W., 1984. An improved method for determining the regional stress tensor using earthquake focal mechanism data: application to the San Fernando earthquake sequence. J. Geophys. Res., 89, 9305-9320.

Gooding, P.J., Kuhnhenn, G.L. and Kiefer, J.D., 1988. Depositional environments and reservoir characteristics of the Lower Ordovician Knox Group and the Middle Ordovician Wells Creek Dolomite and High Bridge Group, Cumberland County, south-central Kentucky. In*: R. Smosna (Editor), A walk through the Paleozoic of the Appalachian Basin. Am. Assoc. Petro. Geologist Eastern Section Meeting., Core Workshop Guidebook, 19-29.

Grasso, J.R., 1992. Mechanics of seismic instabilities induced by recovery of hydrocarbons. Pure Appl. Geophys., 139, 507-534.

Grasso, J.R. and Wittlinger, G., 1990. Ten years of seismic monitoring over a gas field. Bull. Seism. Soc. Am., 80, 450-473.

Hamilton-Smith, T., 1995. Stress, seismicity and structure of shallow fractured carbonate reservoirs of Clinton County, Kentucky.: Final report for Los Alamos National Laboratory: Kentucky Geological Survey Open-File Report, OF-95-02, 143p.

Hamilton-Smith, T., Nuttall, B.C., Gooding, P.J., Walker, D. and Drahovzal, J.A., 1990. High-volume oil discovery in Clinton County, Kentucky. Kentucky Geological Survey, Series 11, Information Circular 33.

Hanks, T.C. and Kanamori, H., 1979. A moment magnitude scale. J. Geophys. Res., 84, 2348-2350.

Harding, T.P., 1974. Petroleum traps associated with wrench faults. Am. Assoc. Petro. Geologist Bull., 58, 1290-1304.

Harding, T.P., 1990. Identification of wrench faults using subsurface structural data: Criteria and pitfalls. Am. Assoc. Petro. Geologist Bull., 74, 1590-1609.

House, L. and Jensen, B., 1987. Focal mechanisms of microearthquakes induced by hydraulic injection in crystalline rock (abstract). Eos, Trans. Am. Geophys. Union, Fall Meeting.

House, L., Flores, R. and Withers, R., 1996. Microearthquakes induced by a hydraulic injection in sedimentary rock, East Texas. Soc. Explor. Geophys. 66th Annual Meeting, Extended Abstracts.

Keck, R.G. and Withers, R.J., 1994. A field demonstration of hydraulic fracturing for solid waste injection with real-time passive seismic monitoring. SPE paper 28495, presented at 69th Soc. Petro. Eng. Annual Technical Conference and Exhibition, New Orleans, Louisianna.

Laurent, J., Bouteca, M. and Sarda, J.P., 1990. Pore pressure influence in poroelastic behavior of rocks: Experimental studies and results. In: EUROPEC90: Increasing the Margin; European Petroleum Conference, Soc. Petro. Eng., Richardson, Texas, 385-392.

Lewis, R.Q., Sr. and Thaden, R.E., 1962. Geology of the Wolf Creek Dam quadrangle, Kentucky. U.S. Geological Survey Map GQ-177.

Lewis, R.Q., Sr. and Thaden, R.E., 1965. Geologic map of the Cumberland City quadrangle, southern Kentucky. U.S. Geological Survey Map GQ-475.

Niitsuma, H., Chubachi, N. and Takanohashi, M., 1987. Acoustic emission analysis of a geothermal reservoir and its application to reservoir control. Geothermics, 16, 47-60.

Pavlis, G.L. and Booker, J.R., 1980. The mixed discrete-continuous inverse problem: application to simultaneous determination of earthquake hypocenters and velocity structure. J. Geophys. Res., 85, 4801-4810.

Pennington, W.D., Davis, S.D., Carlson, S.M., Dupree, J. and Ewing T.E., 1986. The evolution of seismic barriers and asperities caused by the depressuring of fault planes in oil and gas fields of South Texas. Bull. Seism. Soc. Am., 76, 939-948.

Phillips, W.S., Fairbanks, T.D., Rutledge, J.T. and Anderson, D.W., 1998. Induced microearthquake patterns and oil-producing fracture systems in the Austin Chalk. Tectonophysics, this volume.

Plumb, R.A. and Cox, J.W., 1987. Stress direction in eastern North America determined to 4.5 km from borehole elongation measurements. J. Geophys. Res., 92, 4805-4816.

Reasenberg, P. and Oppenheimer, D., 1985. FPFIT, FPPLOT and FPPAGE: Fortran computer programs for calculating and displaying earthquake fault-plane solutions. U.S. Geological Survey, Open-File Report 85-0739.

Reasenberg, P.A. and Simpson, R.W., 1992. Response of regional seismicity to the static stress changes produced by the Loma Prieta earthquake. Science, 255, 1687-1690.

Roff, A., Phillips, W.S. and Brown, D.W., 1996. Joint structures determined by clustering microearthquakes using waveform amplitude ratios. Int. J. Rock Mech. and Min. Sci. and Geomech. Abstr., 33, 627-639.

Rutledge, J.T., Faibanks, T.D., Albright, J.N., Boade, R.R., Dangerfield, J. and Landa, G.H., 1994a. Reservoir seismicity at the Ekofisk oil field. In: Proceedings EUROCK 94, Rock mechanics in petroleum engineering, Soc. Petro. Eng. / Int. Soc. Rock Mech. International Conference, A. A. Balkema, Rotterdam, 589-595.

Rutledge, J.T., Phillips, W.S., Roff, A., Albright, J.N., Hamilton-Smith, T., Jones, S.K. and Kimmich, K.C., 1994b. Subsurface fracture mapping using microearthquakes detected during primary oil production, Clinton County, Kentucky. SPE paper 28384, presented at 69th Soc. Petro. Eng. Annual Technical Conference and Exhibition, New Orleans, Louisianna.

Schuessler, B.K., Rutledge, J.T. and Phillips, W.S., 1995. Source parameters of induced microearthquakes in a shallow oil reservoir, Clinton County, Kentucky (abstract). Eos, Trans. Am. Geophys. Union, Fall Meeting.

Segall, P., 1989. Earthquakes triggered by fluid extraction. Geology, 17, 942-946.

Segall, P., 1992. Induced stresses due to fluid extraction from axisymmetric reservoirs. Pure Appl. Geophys., 139, 535-560.

Segall, P. and Fitzgerald, S., 1998. A note on induced stress changes in hydrocarbon and geothermal reservoirs. Tectonophysics, this volume.

Segall, P., Grasso, J.R. and Mossop, A., 1994. Poroelastic stressing and induced seismicity near the Lacq gas field, southwestern France. J. Geophys. Res., 99, 15423-15438.

Stacey, F.D., 1969. Physics of the Earth. John Wiley and Sons, Inc., New York.

Stein, R.S., King, G.C.P. and Lin, J., 1992. Change in failure stress on the southern San Andreas fault system caused by the 1992 magnitude = 7.4 Landers earthquake. Science, 258, 1328-1332.

Teufel, L.W., Rhett. D.W. and Farrel, H.E., 1991. Effect of reservoir depletion and pore pressure drawdown on in situ stress and deformation in the Ekofisk field, North Sea. Proc. 32nd U.S. Symposium on Rock Mechanics, Norman, Oklahoma.

Teufel, L.W. and Rhett. D.W., 1992. Failure of chalk during waterflooding of the Ekofisk field. SPE paper 24911, presented at 67th Soc. Petro. Eng. Annual Technical Conference and Exhibition, Washington, D.C.

Theis, C.V., 1935. The relation between the lowering of the piezometric surface and the rate and duration of discharge of a well using groundwater storage. Trans. Am. Geophys. Union, 2, 519-524.

Vinegar, H.J., Wills, P.B., DeMartini, D.C., Shylapobersky, J., Deeg, W.F., Adair, R.G., Woerpel, J.C., Fix, J.E. and Sorrels, G.G., 1991. Active and passive seismic imaging of a hydraulic fracture in diatomite. SPE paper 22756, presented at 66th Soc. Petro. Eng. Annual Technical Conference and Exhibition, Dallas, Texas.

Warpinski, N.R., Engler, B.P., Young, C.J., Peterson, R., Branagan, P.T. and Fix, J.E., 1995. Microseismic mapping of hydraulic fractures using multi-level wireline receivers. SPE paper 30507, presented at 70th Soc. Petro. Eng. Annual Technical Conference and Exhibition, Dallas, Texas.

Wood, E.B., 1948. The Seventy-six oil pool: Kentucky Geological Survey Open-File Report OF-48-01, 10p.

Yerkes, R.F. and Castle, R.O., 1976. Seismicity and faulting attributable to fluid extraction. Eng. Geol., 10, 151-167.

Zoback, M.L., 1992. Stress field constraints of intraplate seismicity in eastern North America. J. Geophys. Res., 97, 11761-11782.

Zoback, M.L. and Zoback, M.D., 1980. State of stress in the conterminous United States. J. Geophys. Res., 85, 6113-6156.
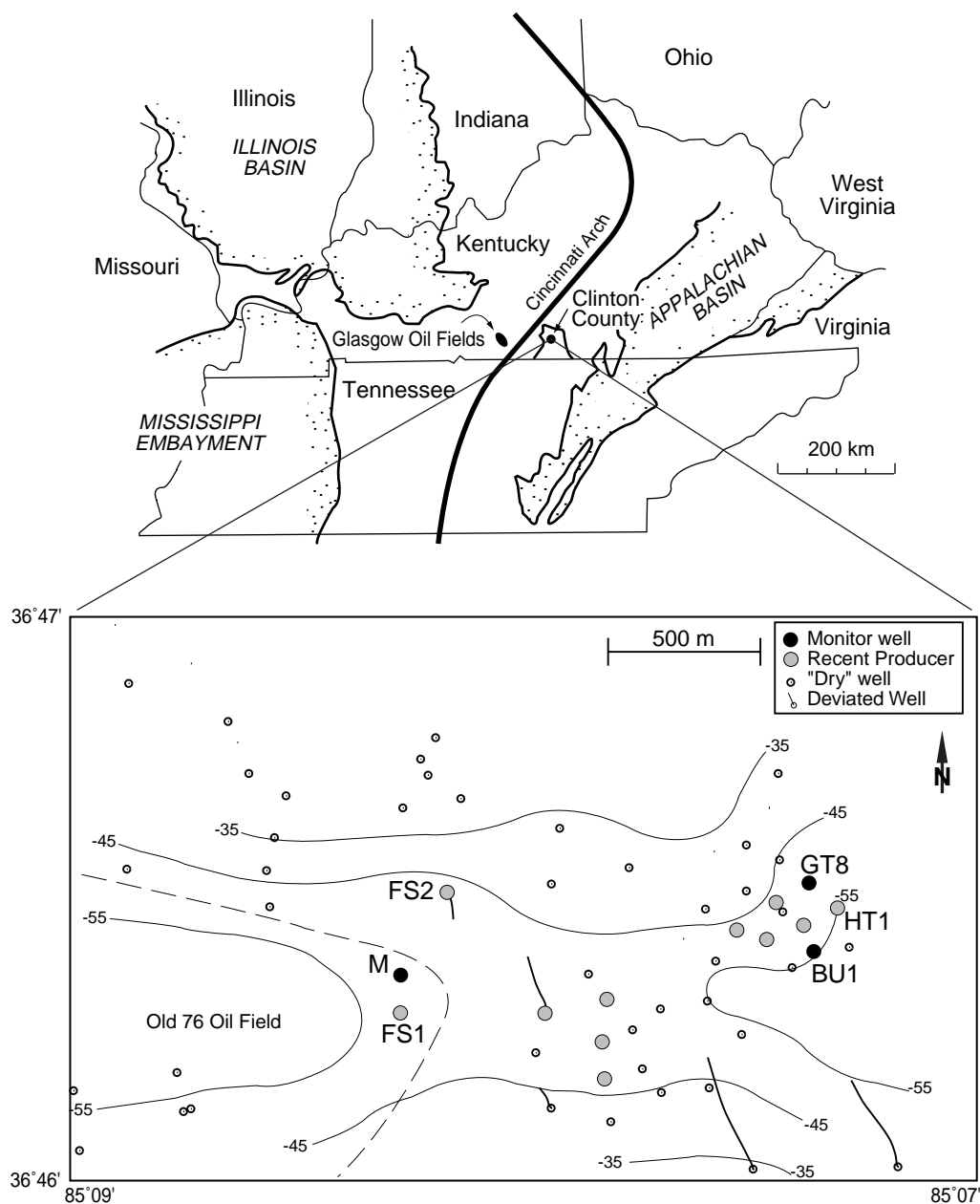
Figure 1. Location map of study area along the Indian Creek syncline. Structure contours show elevation of the top of the High Bridge Group with respect to mean sea level. Contour interval is 10 m. The dashed curve marks the approximate boundary of the old Seventy-Six oil field.
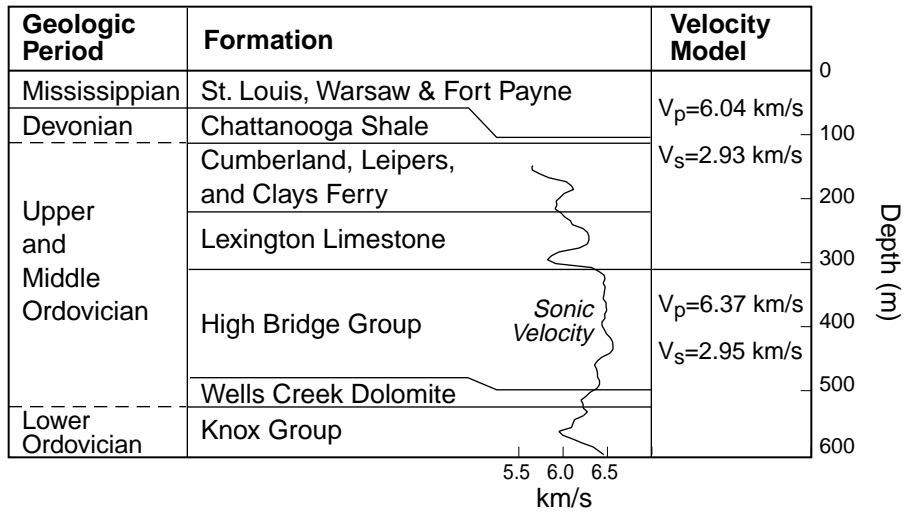
Geologic Period	Formation	Velocity Model	
Mississippian	St. Louis, Warsaw & Fort Payne	V_p=6.04 km/s	
Devonian	Chattanooga Shale		
Upper and Middle Ordovician	Cumberland, Leipers, and Clays Ferry	V_s=2.93 km/s	
	Lexington Limestone		
	High Bridge Group	Sonic Velocity	V_p=6.37 km/s
	Wells Creek Dolomite		V_s=2.95 km/s
Lower Ordovician	Knox Group		

Depth (m): 0, 100, 200, 300, 400, 500, 600

5.5 6.0 6.5
km/s

Figure 2. Geologic section of the study area with P-wave sonic velocity structure and velocity model determined by joint hypocenter-velocity inversion (V_p = P-wave velocity, V_s = S-wave velocity). Dashed divisions in geologic periods are major unconformities. Depths are with respect to well M's wellhead (Figure 1, elevation = 260 m).
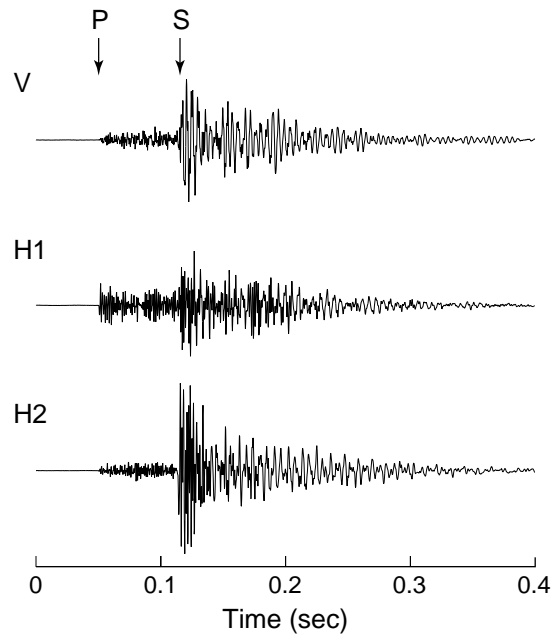
Figure 3. A representative microearthquake 3-component waveform recorded on the lower geophone tool during FS2 monitoring (Table 1). V is the vertical component, H1 and H2 are the two horizontal components. P- and S-wave arrivals are shown. All three traces are plotted at the same relative amplitude scale.
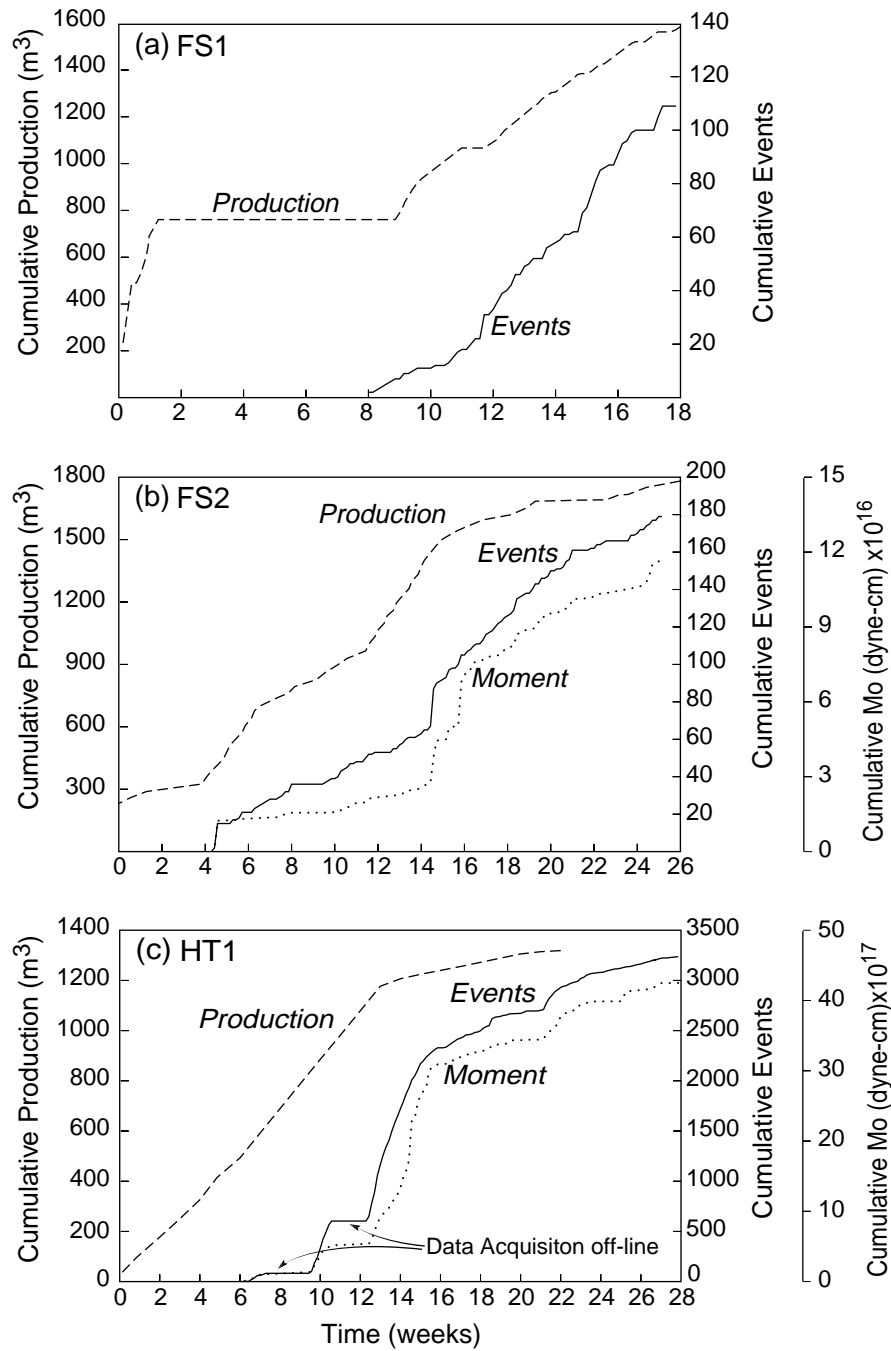
Figure 4. Cumulative production and number of events detected. (b) and (c) also show cumulative seismic moment (Mo). Week zero of all three plots marks the first day of the respective well's production history. Monitoring starts at the earliest position of the cumulative event curves shown for each test.
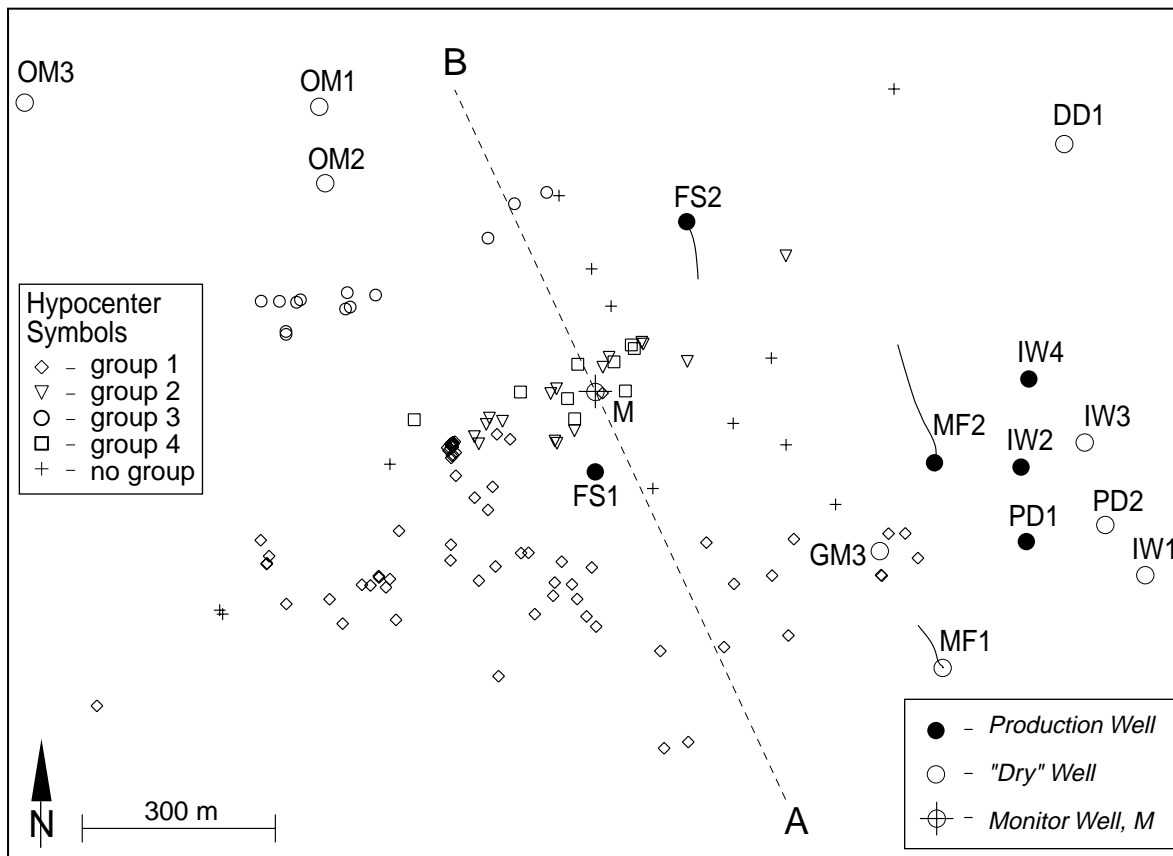
Figure 5. Map view of FS2 microearthquake hypocenters. Deviated well trajectories have well symbols at wellhead locations.
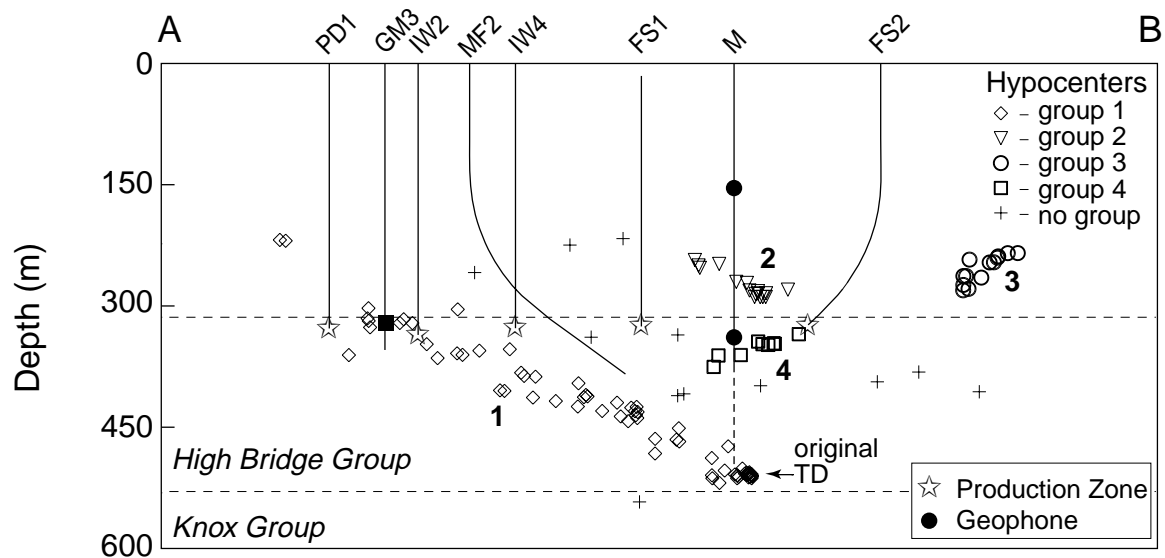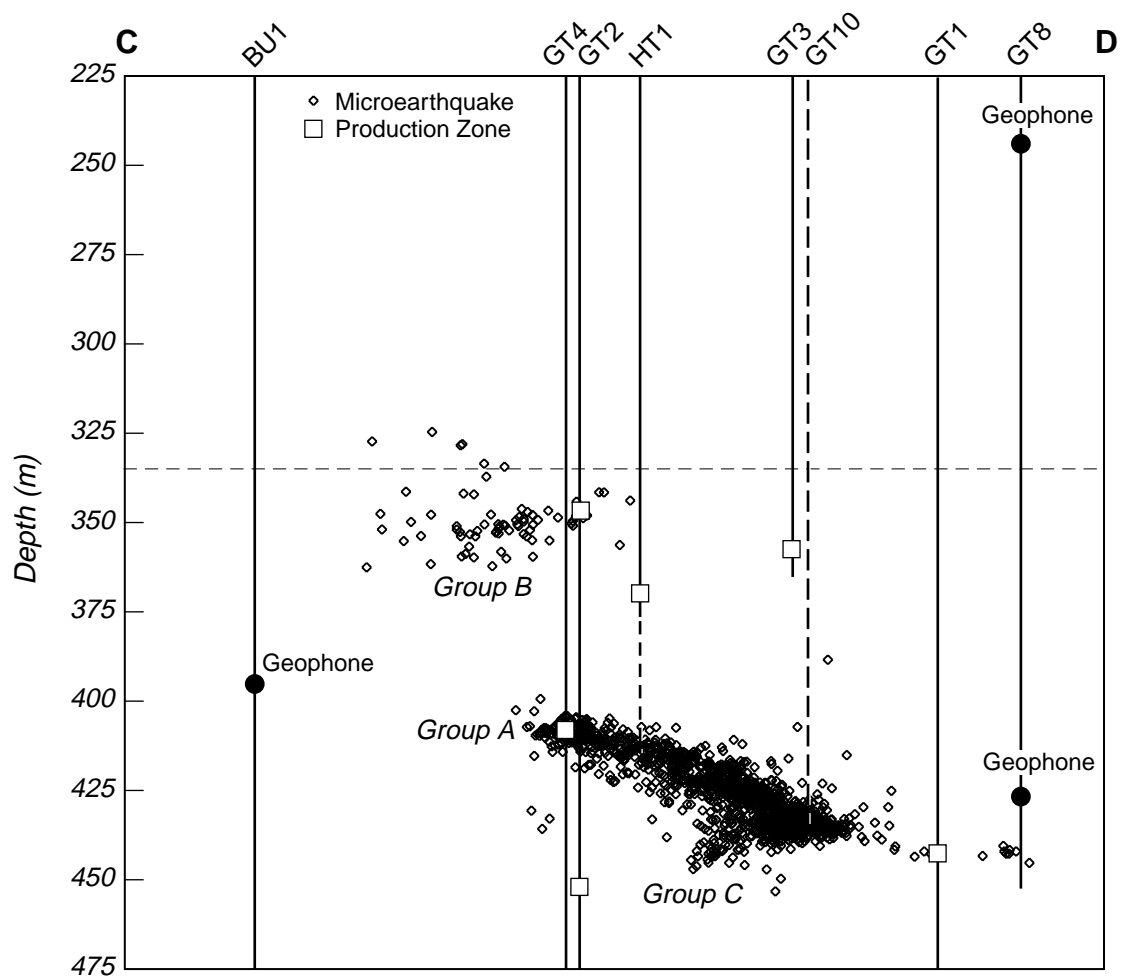
Figure 6. Depth-section projection of FS2 hypocenters along profile A-B of Figure 5.
Projection of production and monitor wells are also shown. Dashed horizontal lines mark
the approximate tops of the High Bridge and Knox Groups. Depth is with respect to wellhead
of M (elevation = 260 m). Well M is shown dashed from an obstruction at 378 m to its original
TD at 489 m. The square symbol along GM3 marks the depth at which brine was produced.
No vertical exaggeration.
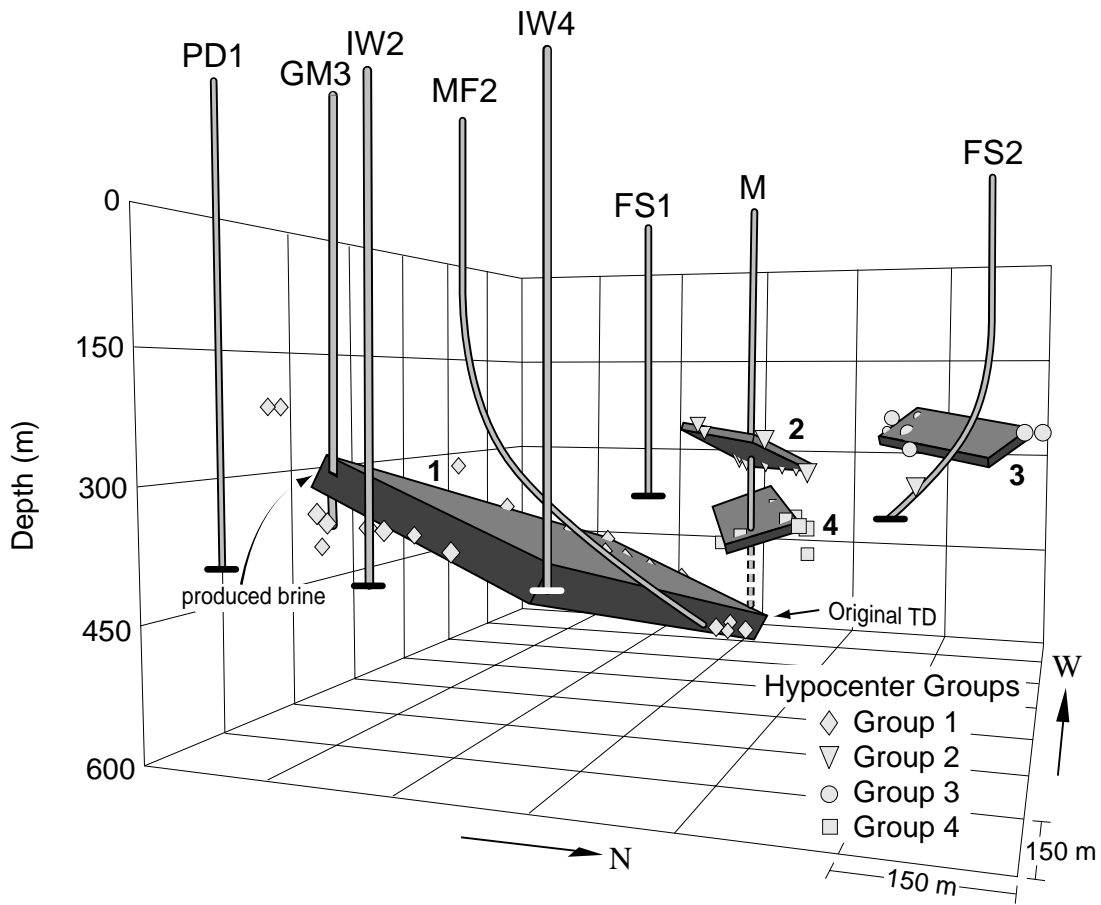
Figure 7. A perspective view of the fracture planes defined by FS2 hypocenter groups 1 through 4. The planar volumes were determined from the eigenvectors fitting the distribution of microearthquake locations within each group. Dimensions of the planar volumes exclude 10% of the extreme outer event locations in each dimension, so that outlying hypocenters do not affect the size and shape of the volumes defined by the majority of events. Hypocenters outside or near the boundaries of the planes are also displayed. Well M is shown dashed from an obstruction at 378 m to its original TD at 489 m. Production intervals are shown with horizontal bars along wellbore terminations. GM3 produced brine where it intersected the group 1 plane.
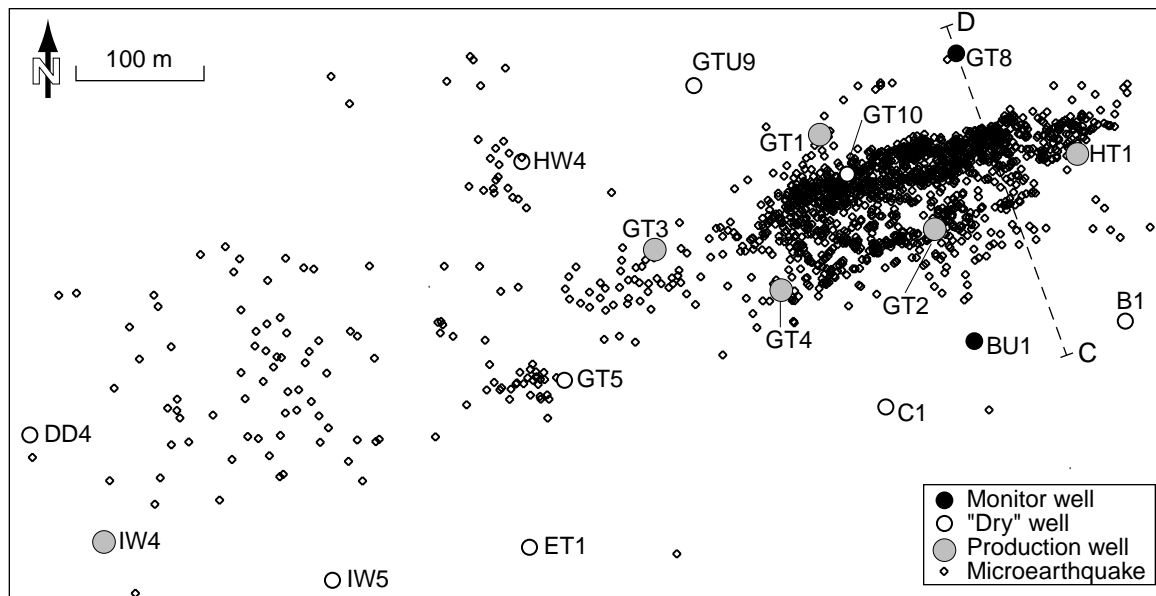
Figure 8. Map view of HT1 microearthquake hypocenters.

Figure 9. Depth-section projection of HT1 hypocenters occurring east of GT3 along profile C-D of Figure 8. Projection of production and monitor wells are also shown. Test well GT10 and deepened interval of HT1 are shown dashed. Dashed horizontal line marks the approximate top of the High Bridge Group. No vertical exaggeration.
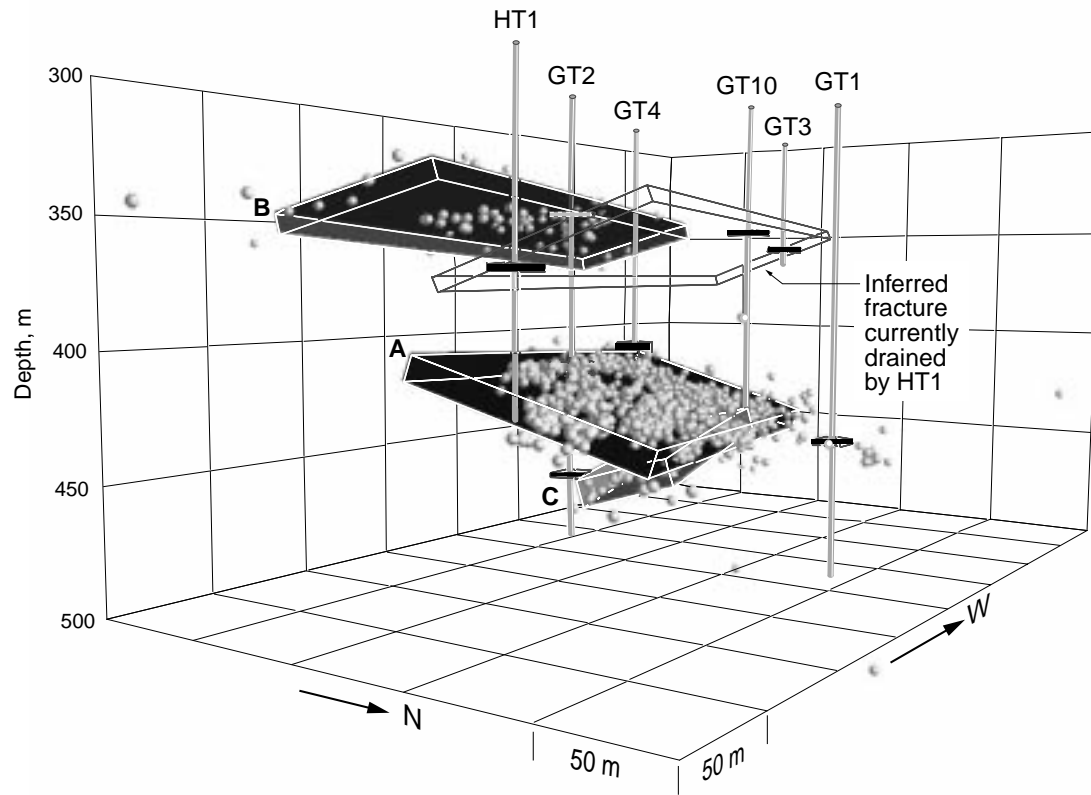
-37-

Figure 10. Perspective view of fracture planes defined by HT1 hypocenter groups A, B
and C. Planar volumes were determined as in Figure 7. Hypocenters within volumes
are also shown. Production intervals of wells are shown with horizontal bars along wellbores.
The upper production interval of GT2, which intersects the group B fracture, is partially obscured.
The inferred fracture drained by HT1 (open box) was determined from the productive intervals of
HT1, GT3 and the log temperature anomaly shown as the horizontal bar along GT10.
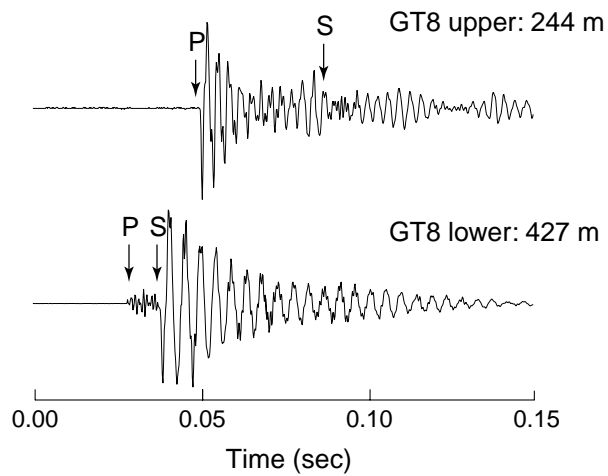
Figure 11. An example of vertical component waveforms associated with the group C fracture recorded on the GT8 upper and lower geophone tools. These events were distinguished by the relatively high P amplitudes and low S amplitudes on the upper tool. The displayed S arrival for the upper tool is the predicted arrival based on the three-station determined location; it cannot be identified on the waveform. The upper trace is amplified 10 times with respect to the lower trace in this display.
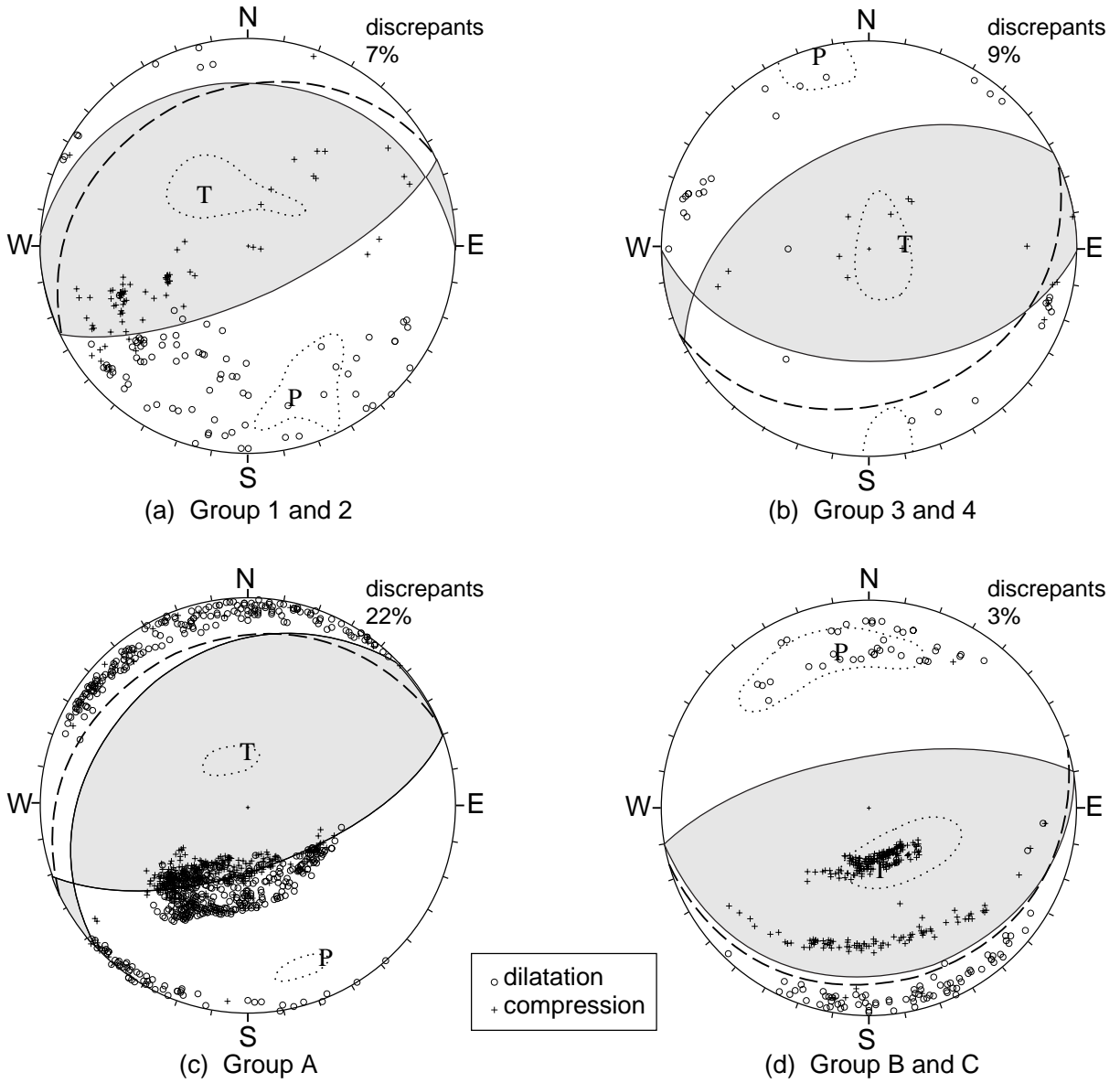
Figure 12. Composite fault plane solutions as equal-area, lower-hemisphere projections. Compressive quadrants are shaded. The dashed curves represent the orientations of the planes determined from the respective hypocenter groups. Average strike and dip of hypocenter-group planes are displayed for the combined-plane solutions. Dotted boundaries around P and T axes show the uncertainty within the 90% confidence limits.
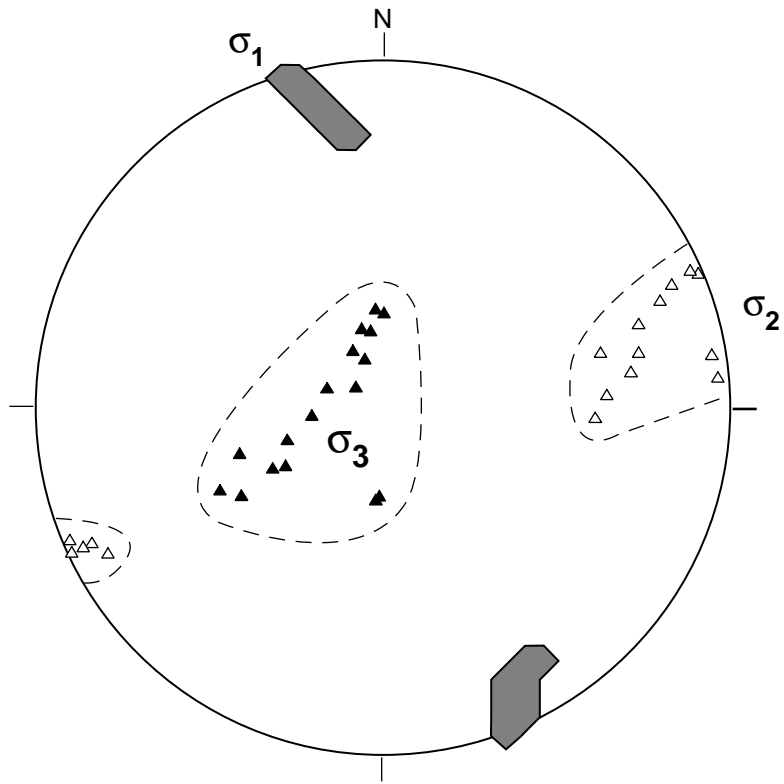
Figure 13. Principle stress orientations determined from the composite focal
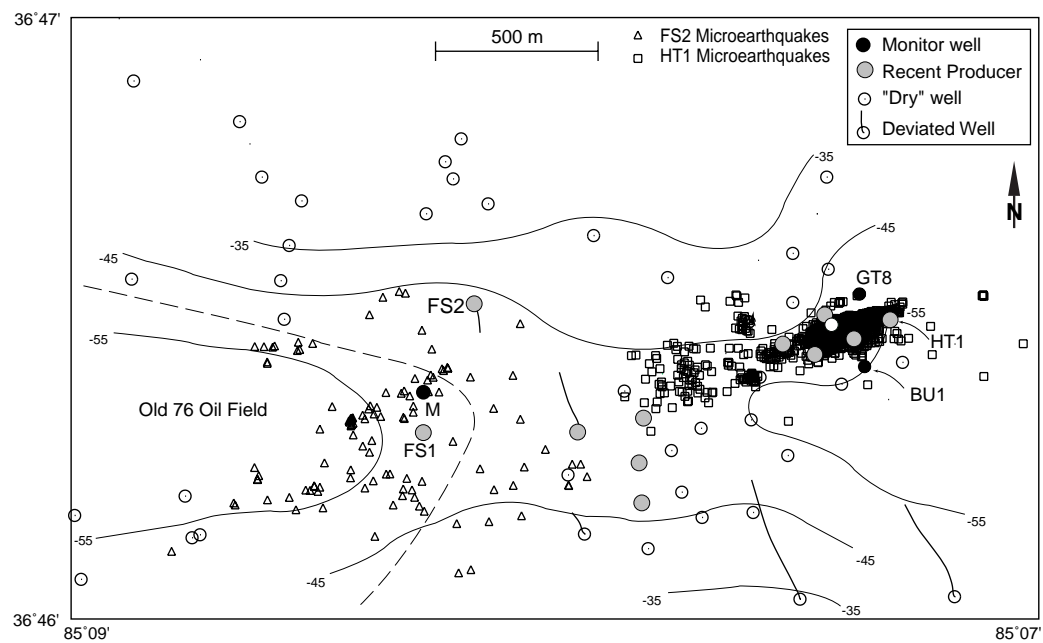mechanisms. Equal-area, lower-hemisphere projection.

Figure 14. Structure map of the top of High Bridge Group with FS2 and HT1 seismicity. Contours show elevation with respect to mean sea level at 10 m intervals. The dashed curve marks the approximate boundary of the old Seventy-Six oil field.
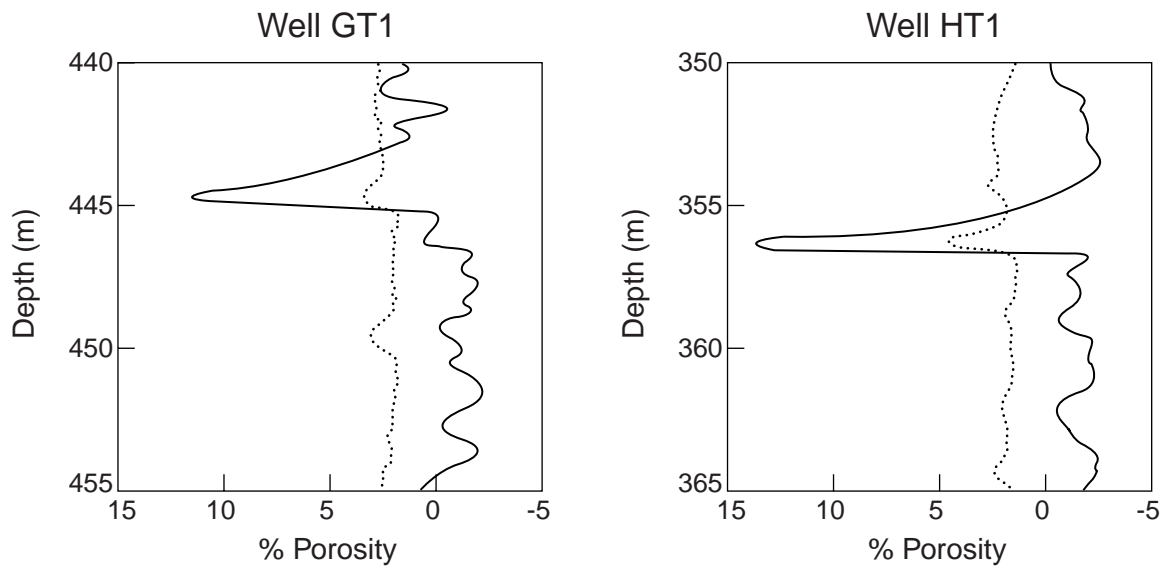
Figure 15. Density-neutron porosity log anomalies for the seismically-active productive interval of GT1 (left) and the seismically-inactive productive interval of HT1 (right). Density porosity log is solid, neutron porosity is dashed.
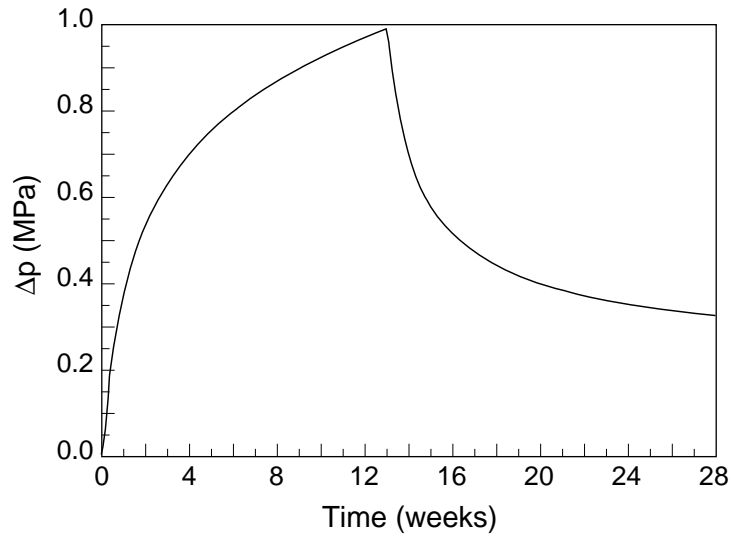
Figure 16. Calculated pressure drop along a drained fracture at 150 m from a production well. Extraction rate starting week zero is 13.7 m^3/day and is reduced to 2.2 m^3/day at start of week 13, corresponding to production rates of HT1 (Figure 4c). For the example shown, the drained volume is treated as a confined aquifer, production interval = 1 m, transmissivity = 5.0×10^{-7} m^2/s, and storage coefficient = 8.0×10^{-6} (Freeze and Cherry, 1979).